Nano Research

Open Access

Research Article

Synergetic catalysis between rare earth-doped g-C_3N_4 and Pt toward enhanced hydrogen oxidation

Yaping Chen[1] ✉, Mengwei Yuan[1,2] ✉, Yuyue Yang[1], Xingtong Liu[1], Liu Lin[1] ✉, Ziheng Liang[1], Rui Gao[1], Zhanpeng Tao[1], Peiyu Wang[1], Hongsong Guo[1], Yifei Liu[1], and Xiaobo Zheng[3] ✉

[1] *Department of Chemistry, Faculty of Arts and Sciences, Beijing Normal University, Zhuhai 519085, China*
[2] *Center for Advanced Materials Research & Faculty of Arts and Sciences, Beijing Normal University, Zhuhai 519087, China*
[3] *Institute for Superconducting and Electronic Materials, Australia Institute for Innovation Material, University of Wollongong, Wollongong, NSW 2522, Australia*

Cite this article: *Nano Research*, **2025**, *18*, 94907349. https://doi.org/10.26599/NR.2025.94907349

ABSTRACT: The tradeoff between hydrogen adsorption binding energy (HBE) and hydroxyl adsorption binding energy (OHBE) critically impacts the sluggish kinetics of hydrogen oxidation reactions (HOR), which significantly impedes the development of anion exchange membrane fuel cells (AEMFCs). Herein, we introduce a novel synergistic catalysis system composed of single rare earth atoms (such as Tb, Ho, Gd, and Er) doped into graphitic carbon nitride (GCN) supported on Pt nanoparticles (GCN-RE-Pt) to balance the tradeoff between HBE and OHBE, thereby enhancing HOR kinetics. In this system, the single rare earth atoms could promote the adsorption of hydroxyl species (OH_{ad}), facilitating hydrogen oxidation and water generation, and induce a surface charge redistribution in GCN, which modulates the electronic structure of the Pt active centers and optimizes the binding energy of adsorbed hydrogen (H_{ad}). As a proof of concept, the optimal GCN-Tb-Pt electrocatalyst achieved a kinetic current density of 12.67 mA·cm^{-2} at an overpotential of 50 mV, which is markedly higher than that of GCN-Pt (6.49 mA·cm^{-2}) and commercial Pt/C (7.28 mA·cm^{-2}). This work opens new avenues for the rational design of highly efficient alkaline HOR catalysts through single rare earth atoms modulating synergistic catalysis.

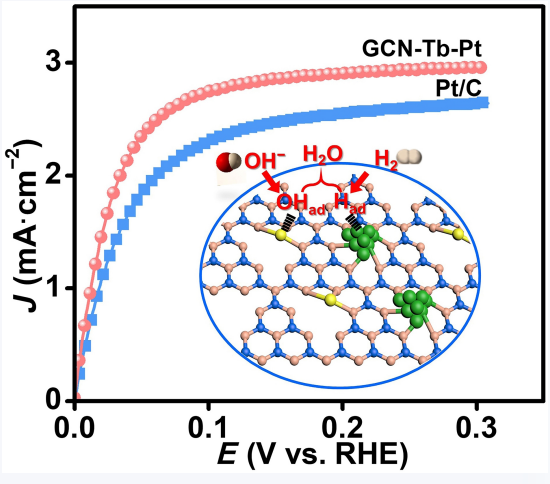

KEYWORDS: hydrogen oxidation reaction, synergistic catalysis, rare metal, platinum

1 Introduction

Due to the significant depletion of fossil fuels and the resulting climate challenges, it is crucial to urgently develop clean and renewable energy technologies [1–4]. However, the intermittent, unpredictable, and non-continuous nature of these energy sources necessitates advancements in energy conversion technologies. Among them, anion exchange membrane fuel cells (AEMFCs) rely crucially on research into catalysts for the hydrogen oxidation reaction (HOR) in alkaline media [5–8]. Platinum (Pt)-based catalysts are among the most effective HOR catalysts due to their exceptional catalytic activity. However, their performance in alkaline conditions is compromised by high hydrogen adsorption binding energy (HBE) and insufficient hydroxyl adsorption energy, leading to sluggish HOR kinetics [8–11]. Researchers have developed many strategies such as alloying and heterostructure engineering to enhance their HOR performance. Alloying Pt with other metals and developing heterostructures are considered effective strategies to tune the electronic structure and d-band center of Pt active sites, thereby optimizing HBE and enhancing the kinetics of HOR [12–15].

In addition to optimizing HBE on Pt active sites, the oxidation of adsorbed hydrogen (H_{ad}) also plays a critical role in enhancing the kinetics of the HOR and facilitating water formation. Typically, in alkaline media, H_{ad} intermediates must couple with OH_{ad} species to form water, a process explained by the bifunctional OH binding

Received: January 18, 2025; **Revised:** March 3, 2025
Accepted: March 4, 2025

✉Address correspondence to Yaping Chen, chenyaping@bnu.edu.cn; Mengwei Yuan, mwyuan@mail.bnu.edu.cn; Liu Lin, linliu@mail.bnu.edu.cn; Xiaobo Zheng, xiaobo5412@163.com

energy (OHBE) theory [10, 16]. This theory emphasizes the cooperative adsorption of H_{ad} and OH_{ad} at two distinct active sites, where H_{ad} is oxidized by OH_{ad} species from synergistic adjacent sites, thus promoting the HOR [17–18]. Therefore, balancing the tradeoff between HBE and OHBE is of pivotal significance to enhancing the alkaline HOR kinetics.

To achieve this aim, Pt is generally alloyed with oxyphilic metals, leveraging the bifunctional mechanism to improve catalytic activity [19–20]. For example, PtRu alloys exhibit outstanding HOR activity in alkaline media by enhancing OH_{ad} adsorption, thanks to the oxyphilic nature of ruthenium (Ru) [5, 18, 21]. However, challenges persist regarding the durability of PtRu alloys, as they are susceptible to oxidation-induced passivation at high potentials. Recent research has shown a growing interest in the synergistic effects between Pt and non-noble metals, specifically 3d transition metals such as Fe, Co, Ni, and Cu, as well as their oxides [22–26]. These metals or oxides can modulate the electronic states of Pt active centers, thereby enhancing intrinsic activity and facilitating the adsorption of OH species. However, the complexity of their structures and coordination chemistry complicates efforts to clarify the catalytic mechanisms and establish definitive structure-activity relationships. More recently, several studies have suggested that alloying Pt with rare earth (Pt-RE) displays lower alloying energy, providing these alloys with kinetic stability against dissolution [27, 28]. Also, when rare-earth atoms are hybridized with Pt, the unique occupancy of 4f orbitals and the La contraction effect characteristic of rare earth can influence the electronic structure of Pt-RE hybrids, potentially optimizing the H_{ad} adsorption and desorption of Pt active sites. Besides, the vacant orbitals of the RE element as a Lewis acid can selectively absorb OH^-, which helps to increase the concentration of OH^- near the Pt active sites, thereby enhancing the overall HOR performance [29–31]. Moreover, single atom catalysts have demonstrated their superiority in various electrocatalytic reactions, including HER and HOR, and have made significant progress [32–36]. However, research on rare earth-based single atom catalysts is relatively limited, particularly in the application of HOR. Therefore, exploring their potential in HOR and unveiling the underlying mechanisms is of great significance.

Herein, we introduce oxyphilic rare earth atoms as effective promoters for HOR in alkaline media. These rare earth atoms are doped into graphitic carbon nitride (GCN) nanosheets supported on Pt nanoparticles (GCN-RE-Pt) to balance the tradeoff between HBE and OHBE, thereby enhancing HOR kinetics. The presence of Tb species facilitates the charge redistribution within the GCN-Tb matrix, efficiently modulating the electronic states of Pt active sites, optimizing the binding energy of adsorbed hydrogen. More importantly, the Tb atoms also assist in the adsorption of OH_{ad} species, helping to oxidize adsorbed H_{ad} intermediates on adjacent Pt active sites. Benefitting from their synergistic interactions, the GCN-Tb-Pt catalysts exhibit remarkable activity and decent durability in the HOR.

2 Experimental

2.1 Materials preparation

2.1.1 *The synthesis and functionalization of GCN*

The melamine (1 g) was placed in a covered porcelain boat and calcined at 550 °C for 2 h in an air atmosphere, with a heating rate of 2.3 °C·min^{-1}. After calcination, the resulting powder was ultrasonicated in 6 mol·L^{-1} hydrochloric acid (HCl) for 1 h and then stirred at room temperature for 4 h. The mixture was subsequently washed repeatedly with deionized water (DIW) seven times until the wash water became neutral. Finally, the material was transferred to a convection drying oven set at 60 °C and dried overnight to obtain GCN.

2.1.2 *The synthesis of GCN-Tb*

180 mg of GCN and 0.06 mmol of $Tb(NO_3)_3{\cdot}6H_2O$ were dispersed in 10 mL of deionized water and ultrasonicated for 3 h. After ultrasonication, the mixture was freeze-dried for 48 h to obtain GCN-Tb. The obtained GCN-Tb was then divided into three portions, and each portion was placed in a covered porcelain boat. These boats were transferred into a tube furnace and heated in an Ar/H_2 atmosphere at a rate of 5 °C·min^{-1} until a temperature of 450 °C was reached, followed by calcination for 3 h. After calcination, the samples were stirred in 1 mol·L^{-1} hydrochloric acid at room temperature for 30 min. The samples were then washed by centrifugation with DIW seven times until the pH became neutral. Finally, the samples were placed in a convection drying oven set at 60 °C and dried overnight to obtain GCN-Tb.

The synthesis of other rare earth doped GCN supports (GCN-Ho, GCN-Gd, and GCN-Er) followed the same procedure as that for GCN-Tb-Pt, except that GCN was used instead of GCN-Tb.

2.1.3 *The synthesis of GCN-Tb-Pt*

18 mg of GCN-Tb was added to a mixture of 20 mL of ethylene glycol and 15 mL of deionized water. 120 μL of 0.2 mol·L^{-1} chloroplatinic acid was then incorporated into the solution. The mixture was ultrasonicated for 2 h to ensure thorough dispersion, and then transferred to an oil bath. The mixture was heated while stirring at 120 °C for 2 h. After the reaction, the mixture was allowed to cool to room temperature. The product was washed by centrifugation twice with DIW, followed by two additional washes with anhydrous ethanol. Finally, the product was placed in a vacuum drying oven set at 60 °C and dried overnight to obtain GCN-Tb-Pt.

The preparation processes for other GCN-Ho-Pt, GCN-Gd-Pt, and GCN-Er-Pt electrocatalysts were identical to those for GCN-Tb-Pt. The synthesis of GCN-Pt followed the same procedure as that for GCN-Tb-Pt, except that GCN was used instead of GCN-Tb.

2.2 Characterizations

X-ray diffraction (XRD) measurements were conducted on a Bruker D8 ADVANCE diffractometer (λ = 1.5406 Å, 40 mA, 40 kV, step size of 0.02°·s^{-1}). Transmission electron microscopy (TEM) images were acquired with a JEOL JEM-2010 microscope at a working voltage of 200 kV. X-ray photoelectron spectroscopy (XPS) tests were carried out on a Thermo Scientific K-Alpha instrument with monochrome Al Kα ($h\nu$ = 1486.6 eV) as the X-ray excitation source. Fourier transform infrared (FT-IR) spectra were acquired on a Thermo Nicolet IS-20 instrument.

2.3 Electrochemical measurements

Electrochemical measurements were conducted using a CHI760E electrochemical workstation (Chenhua, Shanghai) equipped with a rotating disk electrode from Pine Research Instruments, USA. All measurements were performed in a 0.1 M KOH aqueous solution The counter electrode consisted of a platinum plate (0.5 cm ×

0.5 cm), while the reference electrode was an Hg/HgO electrode (in 1 M KOH solution). Working electrodes were prepared by uniformly depositing catalyst inks onto the polished surface of a glassy carbon electrode, with a mass loading of 200 μg·cm^{-2} for all samples. To prepare the catalyst inks for all synthesized samples and commercial Pt/C, 2 mg of the obtained catalysts were combined with 0.5 mg of Vulcan XC-72 carbon black in a solution containing 16 μL of Nafion solution (Alfa Aesar, 5 wt.%), 384 μL of DIW, and 100 μL of isopropanol (IPA). This mixture was subjected to ultrasonication for 2 h to ensure uniformity.

Before linear sweep voltammetry (LSV), the working electrode was firstly cycled between −0.1 and −0.3 V vs. RHE at a scan rate of 50 mV·s^{-1} for 10 cycles to activate the catalysts. LSV curves were carried out in H_2-saturated 0.1 M KOH solution with 95% *iR* correction and recorded at a rotation speed of 1600 rpm with a scanning rete of 1 mV·s^{-1}. The durability CO tolerance test was performed at a constant voltage test (0.1 V vs. RHE) with a CO concentration of 164 ppm in H_2-saturated 0.1 M KOH solution.

CO stripping test: CO was introduced in a CO-saturated 0.1 M KOH for 10 min to allow for CO adsorption with an amperometric *i*–*t* test at 0.1 V vs. RHE. Subsequently, the electrode was performed by cyclic voltammetry (CV) for two cycles in an Ar-saturated 0.1 M KOH solution to facilitate CO desorption at a scan rate of 200 mV·s^{-1}.

Electrochemical active surface area (ECSA) was obtained using the hydrogen underpotential deposition (H_{UPD}) method. Cyclic voltammetry tests were conducted in an Ar-saturated 0.1 mol·L^{-1} KOH solution at a scan rate of 50 mV·s^{-1}, with a voltage range of −0.095 to 1.195 V (vs. RHE). The calculation of ECSA was determined according to the following formula

$$\mathrm{ECSA}\ (\mathrm{cm}^2\cdot\mathrm{mg}^{-1}) = \frac{Q_{\mathrm{H-upd}}\ (\mathrm{C})}{0.21\ (\mathrm{mC}\cdot\mathrm{cm}^{-2}) \times M_{\mathrm{Pt}}\ (\mathrm{g})} \quad (1)$$

where $Q_{H\text{-}upd}$ is the charge of the adsorbed hydrogen, 0.21 mC·cm^{-2} is the charge associated with the adsorption of hydrogen on a monolayer of Pt, and M_{Pt} is the mass of Pt.

The kinetic current (J_k) was calculated by the Koutecky–Levich equation

$$\frac{1}{J} = \frac{1}{J_k} + \frac{1}{J_d} \quad (2)$$

where J stands for the measured current and J_d represents the diffusion limited current, which can be calculated from the following equation

$$J_d = J_l\left(1 - e^{-\frac{2F}{RT}\eta}\right) \quad (3)$$

where J_l is the limiting diffusion current density, F is Faraday's constant (96,485 C·mol^{-1}), η is the overpotential, R is the gas constant (8.314 J·mol^{-1}·K^{-1}), and T is the temperature (298.15 K).

The exchange current density normalized to the electrode area (J_0) is obtained by fitting J_k and η using the Butler–Volmer equation

$$J_k = J_0\left(e^{\frac{\alpha F}{RT}\eta} - e^{\frac{(\alpha-1)F}{RT}\eta}\right) \quad (4)$$

where α represents the charge transfer coefficient.

3 Results and discussion

The XRD patterns of GCN and GCN-Tb are presented in Fig. 1(a).

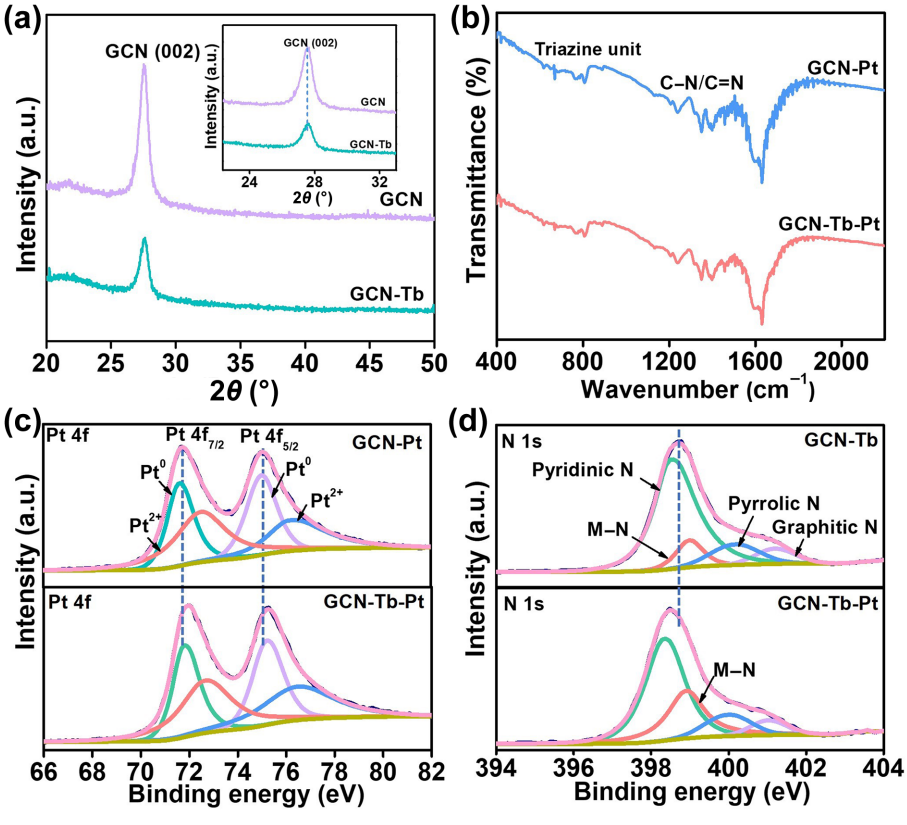

Figure 1 (a) XRD patterns of GCN and GCN-Tb, with the inset showing a magnified view of the GCN (002) peak. (b) FT-IR spectra of GCN-Tb and GCN-Tb-Pt. High-resolution XPS spectra for (c) Pt 4f and (d) N 1s of GCN-Tb and GCN-Tb-Pt, respectively.

The (002) peak corresponds to the interlayer stacking reflection of the conjugated aromatic system in GCN. Notably, the peak positions of GCN-Tb exhibit a slightly positive shift compared to GCN, suggesting that there is an expansion in interlayer spacing after the introduction of Tb into GCN. Additionally, the peak intensities of GCN-Tb are lower than those of GCN, suggesting that the incorporation of Tb may lead to reduced crystallinity [37, 38]. The presence of the Pt (111) and Pt (200) peaks confirms the successful loading of Pt in the GCN-Pt and GCN-Tb-Pt (Fig. S1(a) in the Electronic Supplementary Material (ESM)) [39, 40]. The FT-IR spectra of GCN, GCN-Tb, and GCN-Tb-Pt display a distinct stretching peak at 810 cm^{-1} which can be associated with the triazine ring (Fig. 1(b) and Fig. S2 in the ESM). Furthermore, stretching peaks corresponding to the heptazine ring are observed in the range of 1200–1600 cm^{-1} [41, 42]. These findings indicate that the doping of terbium does not alter the ring structure of GCN, thereby ensuring the structural stability of the GCN-Tb support.

The chemical composition and valence states of the GCN-Tb, GCN-Pt, and GCN-Tb-Pt catalysts were analyzed by XPS. The XPS survey spectrum verifies the coexistence of C, N and Pt elements in the GCN-Tb-Pt sample (Fig. S3 in the ESM). The Tb XPS signal is not obviousdetected due to its low concentration. Figure 1(c) shows the Pt 4f spectra for both GCN-Pt and GCN-Tb-Pt. Notably, the binding energy of Pt $4f_{7/2}$ and Pt $4f_{5/2}$ in GCN-Tb-Pt positively shifts from 71.7 and 75.1 to 71.9 and 75.2 eV, respectively, as compared with GCN-Pt. The shift indicates a decrease in electron density around the Pt sites following the incorporation of Tb single atoms into the GCN substrate [43]. This binding energy shift is closely related to the adsorption and desorption behavior of OH_{ad}. The upshift in Pt 4f binding energy may enhance the bonding energy between OH_{ad} and the Pt active sites, facilitating the desorption of OHad and promoting the oxidation of hydrogen adsorbates [42, 44]. Additionally, Fig. 1(d) shows the N 1s spectra for GCN-Tb-Pt and GCN-Tb, which can be deconvoluted into different nitrogen species: pyridinic N, pyrrolic N, graphitic N, and metal-N [45]. This indicates interfacial bonding between N sites and Pt/Tb atoms. A negative shift of 0.2 eV in the N 1s spectrum is observed after the deposition of Pt nanoparticles, suggesting charge transfer from Pt to N and further indicating the formation of Pt–N bonds. The presence of Pt–N bonds between Pt and the GCN support is confirmed by comparing the N 1s spectra of GCN-Pt with that of the GCN support (Fig. S4 in the ESM). Similarly, Tb–N bonding is validated by comparing the N 1s spectra of GCN-Tb with that of the GCN support (Fig. S5 in the ESM). The formation of Tb–N bonds leads to charge redistribution between Tb and the GCN substrate, thereby modulating the electronic structure of the deposited Pt nanoparticles. Additionally, the mass ratios of Pt were determined to be 17.4 wt.% for GCN-Pt and 12.9 wt.% for GCN-Tb-Pt, as measured by inductively coupled plasma-optical emission spectrometry (ICP-OES) with mass spectrometry. Furthermore, the content of Tb in GCN-Tb-Pt reached 0.16 wt.%.

High-angle annular dark-field scanning transmission electron microscopy (HAADF-STEM) images of GCN-Tb demonstrate an even distribution of Tb single atoms across the GCN supports (Fig. 2(a)). The TEM images of GCN-Tb-Pt and GCN-Pt display that the Pt nanoparticles are uniformly distributed on the GCN-Tb and GCN supports (Figs. 2(a) and 2(b) and Fig. S6 in the ESM). The observed *d*-spacing of 0.23 nm corresponds to the (111) crystal plane of Pt. Additionally, the elemental mapping of GCN-Tb-Pt (Figs. 2(e) and 2(f)) confirms the uniform distribution of C, N, Pt, and Tb elements within the composite. A semiquantitative analysis of the elemental content was performed using energy disperse spectroscopy (EDS), and the result reveals that the Tb content is 0.18 wt.%, while the Pt content is 7.61 wt.%.

The HOR performance of catalysts was evaluated using a rotating disk electrode (RDE) in a three-electrode system. GCN-Tb-Pt shows the lowest onset potential and the highest current density as compared with those of the GCN-Pt and commercial Pt/C catalysts, indicating that the doping of Tb species plays a crucial role in promoting the activity of GCN-Tb-Pt catalyst (Fig. 3(a)). The LSV curves for GCN-Tb-Pt, GCN-Pt, and Pt/C at various rotation speeds are presented in Fig. 3(b), and Figs. S7(a) and S8(a) in the ESM. As the rotation speed increases, the current density also rises, indicating enhanced mass transfer capabilities. The Koutecky-

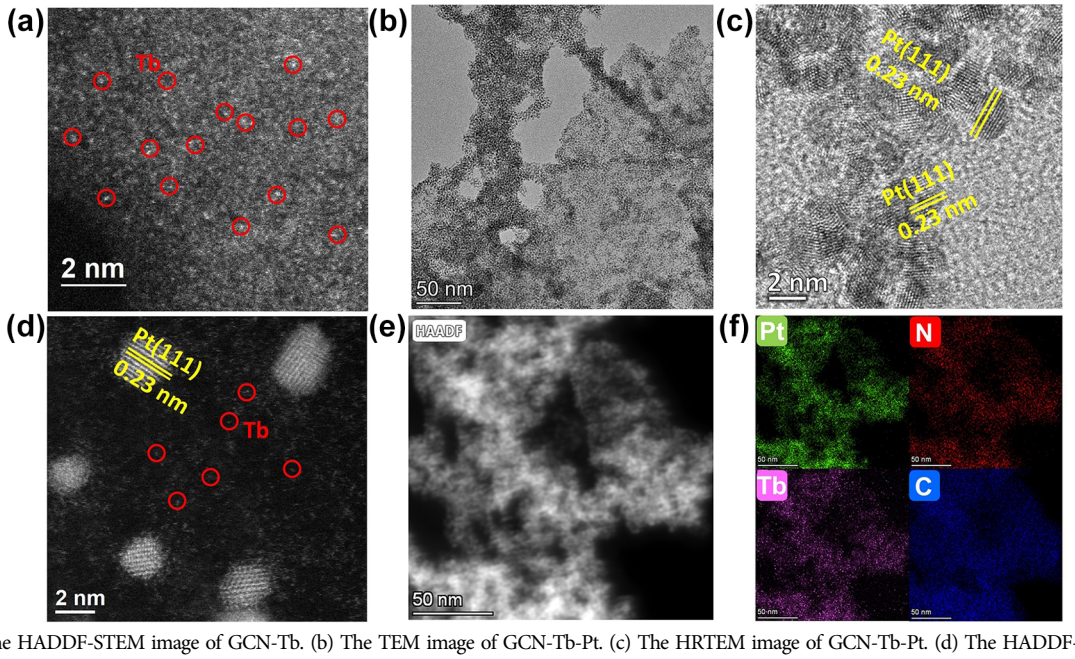

Figure 2 (a) The HADDF-STEM image of GCN-Tb. (b) The TEM image of GCN-Tb-Pt. (c) The HRTEM image of GCN-Tb-Pt. (d) The HADDF-STEM image of GCN-Tb-Pt. (e) and (f) The STEM EDS mapping of GCN-Tb-Pt.

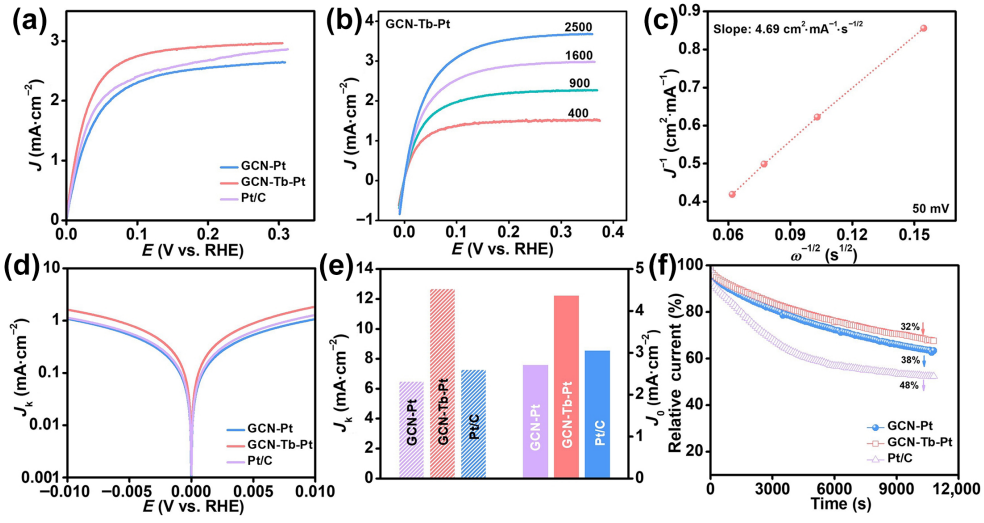

Figure 3 The electrochemical characterization of GCN, GCN-Tb, and GCN-Tb-Pt samples. (a) The LSV curves carried out in 0.1 M KOH at the scan rate of 0.1 mV·s^{-1}. (b) The corresponding Tafel plots. (c) The LSV curve at various rotation rates. (d) The Koutecký–Levich plots at an overpotential of 50 mV. (e) Comparison of j_0 and current density normalized with the Pt mass at an overpotential of 50 mV. (f) Long-term durability performed at 0.1 V (vs. RHE) for 3 h in H_2-saturated 0.1 M KOH.

Levich plots (Fig. 3(c), and Figs. S7(b) and S8(b) in the ESM) reveal a linear relationship between the inverse current density (J^{-1}) and $\omega^{-1/2}$ at 50 mV (vs. RHE). The slopes obtained from the linear fits for GCN-Tb-Pt, GCN-Pt, and Pt/C are 4.69, 5.46, and 5.03 cm^2·mA^{-1}·s$^{-1/2}$, which are close to the theoretical value of 4.87 cm^2·mA^{-1}·s$^{-1/2}$ for the two-electron HOR, confirming that the two-electron HOR reaction is indeed occurring. The Tafel plots illustrate the relationship between the kinetic current J_k and voltage, derived from the Koutecky-Levich equation, shown in Fig. 3(d). This plot further demonstrates that GCN-Tb-Pt enhances the kinetics of the HOR. Figure 3(e) presents the exchange current density J_0, obtained through fitting with the Butler-Volmer equation, alongside the kinetic current density J_k at an overpotential of 50 mV (vs. RHE). The J_0 value for GCN-Tb-Pt is 4.36 mA·cm^{-2}, which exceeds that of Pt/C (3.05 mA·cm^{-2}) and GCN-Pt (2.71 mA·cm^{-2}). Furthermore, GCN-Tb-Pt exhibits a significantly higher kinetic current density of 12.67 mA·cm^{-2}, compared to 7.28 mA·cm^{-2} for Pt/C and 6.49 mA·cm^{-2} for GCN-Pt at 50 mV (vs. RHE). These findings significantly indicate that the introduction of Tb atoms substantially enhances the activity of GCN-Tb-Pt electrocatalysts. Besides, durability tests were performed using the chronoamperometry (CA) method in an H_2-saturated 0.1 M KOH solution at 0.1 V (vs. RHE). As illustrated in Fig. 3(f), after 3 h of testing, the current density of GCN-Tb-Pt decreased by 32.5%, which is significantly lower than the reductions observed for Pt/C (47.7%) and Pt-GCN (36.7%). The enhanced stability can be attributed to the strong interfacial bonds formed between GCN-Tb and Pt nanoparticles, which strengthen the structural stability of the GCN-Tb-Pt catalyst.

To elucidate the mechanism behind the enhanced HOR activity for GCN-Tb-Pt catalyst originating from the synergistic effects of Tb species, CO stripping measurement was conducted to access the binding strength of OH species. As shown in Fig. 4(a), the onset potential of CO stripping for GCN-Tb-Pt catalyst reaches 0.36 V, which is significantly lower than those of GCN-Pt (0.50 V) and Pt/C (0.52 V), suggesting an improved OHBE for the GCN-Tb-Pt sample, thereby facilitating the oxidation of CO. The CO tolerance was further evaluated by the CA test at 0.1 V (vs. RHE) in CO 164 ppm H_2-saturated 0.1 M KOH solution (Fig. 4(b)). Clearly, the current density of GCN-Tb-Pt sample reduces by 27% after 3600 s, while the current density of GCN-Pt and Pt/C catalysts decline by 54% and 55%, respectively. This demonstrates that the incorporation of Tb enhances the OHBE, accelerates the oxidation of CO, and improves the CO resistance. Additionally, the hydrogen underpotential deposition (Hupd) peak of GCN-Tb-Pt (0.208 V) is notably lower than those of GCN-Pt (0.218 V) and Pt/C (0.226 V), as shown in Fig. 4(c), indicating that GCN-Tb-Pt exhibits a weaker HBE at the Pt active sites. The decreased HBE for GCN-Tb-Pt is attributed to the incorporation of Tb atoms, which tunes the electronic redistribution within the GCN matrix, thereby adjusting the electronic structure of the Pt active centers and optimizing the HBE. Furthermore, the GCN-Tb-Pt catalyst presents optimal hydrogen evolution reaction (HER) activity, achieving a current density of 10 mA·cm^{-2} with a driving overpotential of only 73 mV, surpassing that of GCN-Pt (85 mV) and Pt/C (93 mV) at the same current density (Fig. 4(d)).

The impressive HOR performance of GCN-Tb-Pt can be attributed to the unique synergetic catalysis system. In alkaline solutions, the rate-limiting step of the HOR on Pt typically involves the adsorption and oxidation of hydrogen. It has been suggested that OH^- from the alkaline medium can directly participate in the oxidation of adsorbed hydrogen atoms on the Pt surface, following the HBE mechanism. However, a more commonly accepted pathway involves free OH^- reacting with H_{ad} at or near the Pt active sites through a bifunctional mechanism. As shown in Fig. 5(a), Tb atoms can induce local charge redistribution in the GCN-Tb support, which effectively modulates the electronic structure of Pt and enhances the HBE of Pt active centers. More importantly, the presence of Tb atoms could promote the adsorption of OH^- species, facilitating the oxidative removal of H_{ad} and thereby improving the kinetics of the HOR for GCN-Tb-Pt catalysts.

To further validate the general applicability of rare earth atoms in this synergetic catalysis system, we also synthesized other rare earth atom-doped GCN matrices supported Pt nanoparticles (GCN-RE-Pt, RE = Er, Ho, Gd) for the alkaline HOR. The XRD patterns and FTIR spectra have demonstrated the successful synthesis of GCN-RE-Pt (Figs. S9–S11 in the ESM). As shown in Figs. 5(b) and 5(c), the onset potentials (E_{onset}) for the GCN-Er-Pt, GCN-Ho-Pt, and

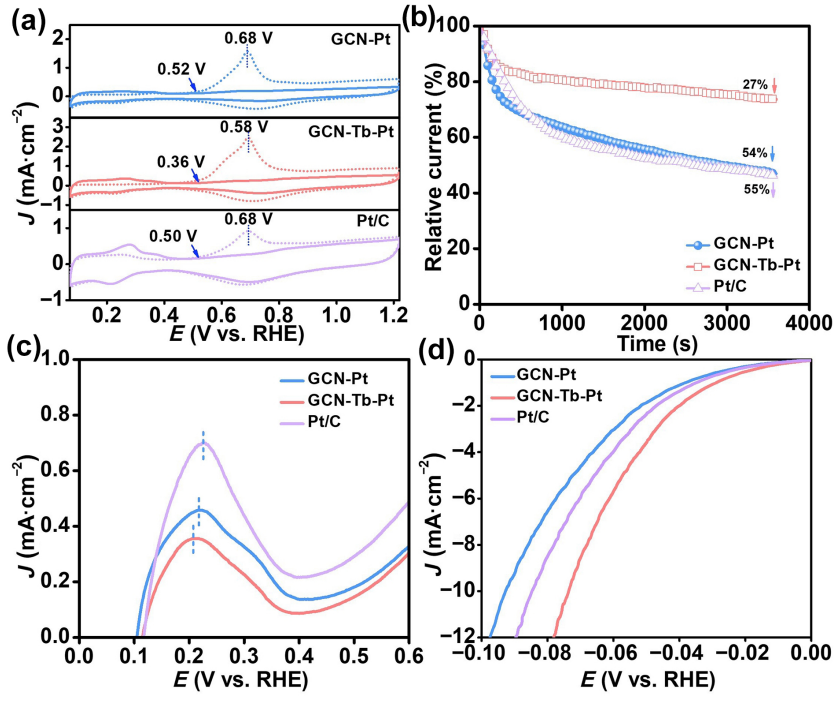

Figure 4 The CO stripping and HER measurement of GCN, GCN-Tb, and GCN-Tb-Pt samples. (a) CV curves in Ar-saturated 0.1 M KOH, showing the desorption of the H_{upd}. (b) CO stripping voltammetry. (c) Relative chronoamperometry response in H_2/10,000 ppm CO-saturated 0.1 M KOH solution at 0.1 V (vs RHE). (d) HER polarization curves in N_2-saturated 0.1 M KOH.

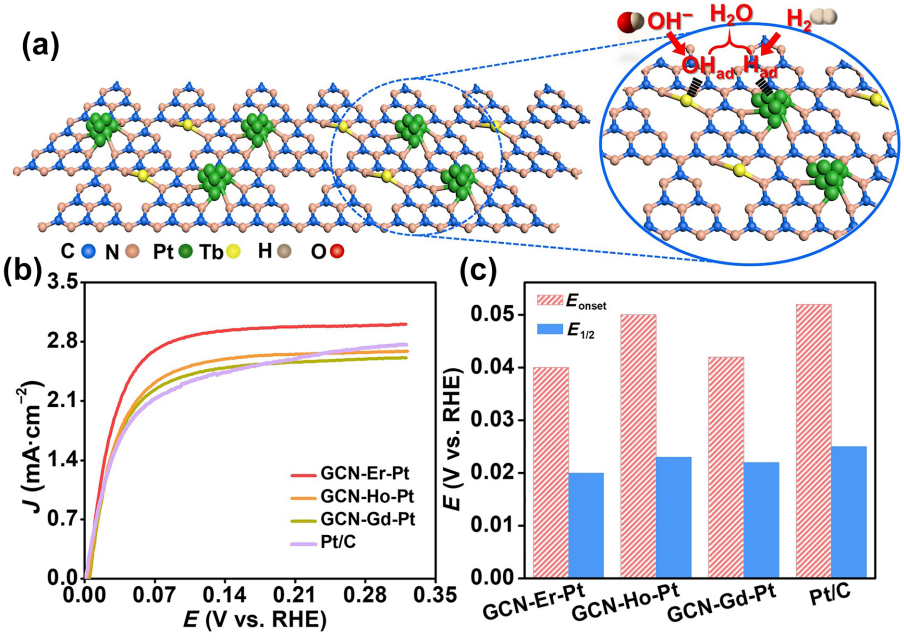

Figure 5 (a) Illustration of synergistically catalytic process between Tb atoms and adjacent Pt sites. (b) The LSV curves at various rotation rates for GCN-RE-Pt and Pt/C. (c) The corresponding onset and half-wave potential.

GCN-Gd-Pt catalysts are 0.04, 0.05, and 0.042 V, respectively, all of which are lower than that of Pt/C (E_{onset} = 0.052 V). Additionally, the half-wave potentials ($E_{1/2}$) for GCN-Er-Pt (0.020 V), GCN-Ho-Pt (0.023 V), and GCN-Gd-Pt (0.022 V) are also notably smaller than that of Pt/C (0.025 V). These results demonstrate that the introduction of single rare-earth atoms into the GCN-RE-Pt catalysis can be an effective strategy to enhance the alkaline HOR performance of Pt through tuning the HBE and OHBE.

To elucidate the enhanced intrinsic activity of GCN-Tb-Pt catalysts for the alkaline HOR, Density functional theory (DFT) calculations were conducted. Figure 6(a) presents the optimized atomic structures of GCN-Pt and GCN-Tb-Pt electrocatalysts. The charge density difference, illustrated in Fig. S12 in the ESM, indicates significant electron transfer from Pt to the GCN-Tb support, agreeing with the XPS results. As shown in Fig. 6(b), the Pt sites in GCN-Tb-Pt (GCN-Tb-Pt@Pt) exhibit an optimal hydrogen adsorption energy (ΔG_H) of −0.46 eV, which is more favorable than that of GCN-Tb-Pt@Tb (−0.67 eV) and GCN-Pt@Pt (−0.49 eV).

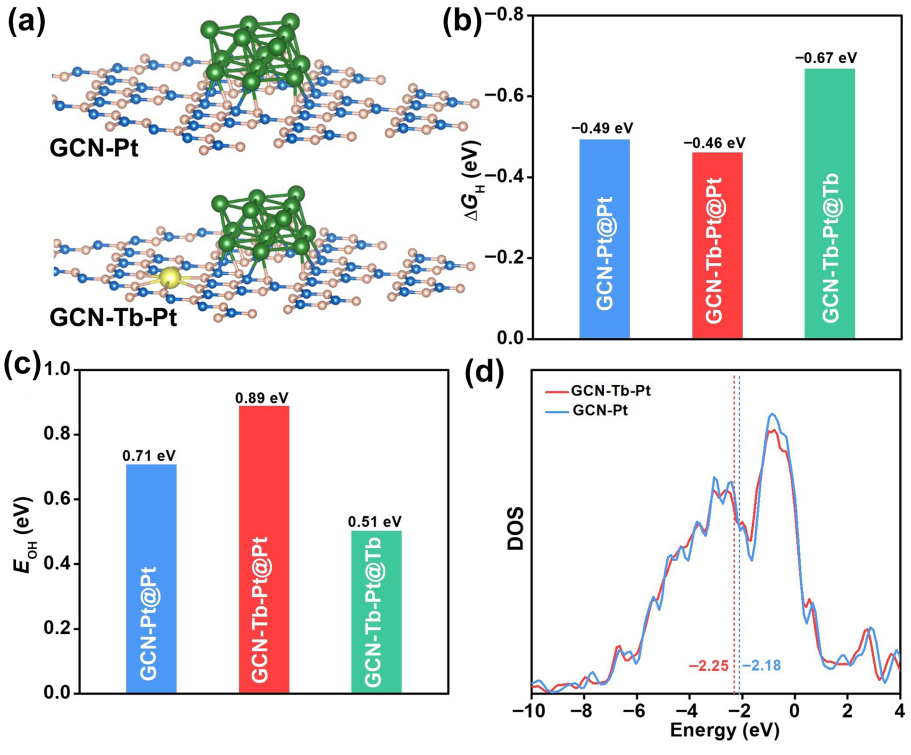

Figure 6 (a) Optimized atomic structures of GCN-Pt and GCN-Tb-Pt electrocatalysts. (b) Free-energy diagram for H adsorption on Pt sites of GCN-Pt and GCN-Tb-Pt, as well as on Tb sites of GCN-Tb-Pt. (c) The binding energy for OH adsorption on Pt sites of GCN-Pt and GCN-Tb-Pt, along with Tb sites of GCN-Tb-Pt. (d) DOS plots of GCN-Pt and GCN-Tb-Pt.

Additionally, GCN-Tb-Pt@Tb demonstrates stronger OH_{ad} adsorption (Fig. 6(c)). Given that OH_{ad} adsorption is a critical factor in the bifunctional OHBE mechanism, the enhanced OH_{ad} binding facilitates greater OH adsorption, which couples with H_{ad} to promote its oxidation and removal [46–48]. This accelerates the Volmer step through the bifunctional OHBE mechanism. Figure 6(d) shows the density of states (DOS) for Pt in both GCN-Pt and GCN-Tb-Pt. In GCN-Tb-Pt, the d-band center of Pt shifts further below the Fermi level compared to GCN-Pt, leading to weaker Pt–H bonds and aligning with the observed lowest ΔG_H. Consequently, the balanced H_{ad} and OH_{ad} adsorption behaviors, driven by the synergistic interaction between adjacent Pt and Tb sites in GCN-Tb-Pt, play a crucial role in enhancing HOR kinetics in alkaline electrolytes.

4 Conclusion

In summary, the introduction of single rare-earth atoms into the GCN-RE-Pt synergistic catalysis system could significantly enhance the HOR performance of Pt via modulating the HBE and OHBE. The rare earth atoms could promote the adsorption of hydroxyl species (OH_{ad}), accelerating the oxidative removal of H_{ad} intermediates and facilitating the formation of water. Furthermore, it could also induce the local surface charge redistribution, which modulates the electronic structure of Pt active sites, optimizing the HBE and enhancing HOR kinetics. The optimized GCN-Tb-Pt shows superior performance, achieving a high kinetic current density at a low overpotential, surpassing both GCN-Pt and commercial Pt/C. This single rare earth atoms-induced synergistic catalysis approach provides a promising strategy for the design of efficient alkaline HOR electrocatalysts.

Electronic Supplementary Material: Supplementary material (the additional XRD patterns, TEM images, XPS survey spectra, fitting results of XPS spectra, LSV curves, and FTIR spectra for the samples) is available in the online version of this article at https://doi.org/10.26599/NR.2025.94907349.

Data availability

All data needed to support the conclusions in the paper are presented in the manuscript and the Electronic Supplementary Material. Additional data related to this paper may be requested from the corresponding author upon request.

Acknowledgements

This work was financially supported by the National Natural Science Foundation of China (No. 52401260), the Australian Research Council (ARC) Discovery Project (No. DP210102215), and the Discovery Early Career Researcher Award (No. DE250100730). L. L. acknowledges the support by the National Natural Science Foundation of China (No. 22302013).

Declaration of competing interest

All the contributing authors report no conflict of interests in this work.

Author contribution statement

Y. P. C.: Data curation, project administration, validation, writing manuscript, experimental design. M. W. Y.: DFT data curation, experimental design. Y. Y. Y.: Experimental administration. X. T. L.:

Data curation. L. L.: Project administration, funding acquisition, writing manuscript. Z. H. L.: Data curation. R. G.: Data curation. Z. P. T.: Experimental administration. P. Y. W.: Data curation. H. S. G.: Data curation. Y. F. L.: Experimental administration. X. B. Z.: Data curation, project administration, validation, writing manuscript. All the authors have approved the final manuscript.

Use of AI statement

None.

References

[1] Gao, Y.; Yang, C. D.; Sun, F. L.; He, D. P.; Wang, X. Q.; Chen, J.; Zheng, X. B.; Liu, R. C.; Pan, H. G.; Wang, D. S. Ligand-tuning metallic sites in molecular complexes for efficient water oxidation. *Angew. Chem., Int. Ed.* **2025**, *64*, e202415755.

[2] Zheng, X. B.; Yang, J. R.; Li, P.; Wang, Q. S.; Wu, J. B.; Zhang, E. H.; Chen, S. H.; Zhuang, Z. C.; Lai, W. H.; Dou, S. X. et al. Ir–Sn pair-site triggers key oxygen radical intermediate for efficient acidic water oxidation. *Sci. Adv.* **2023**, *9*, eadi8025.

[3] Yang, J. R.; Zhu, C. X.; Wang, D. S. A simple organo-electrocatalysis system for the chlor-related industry. *Angew. Chem., Int. Ed.* **2024**, *63*, e202406883.

[4] Glenk, G.; Reichelstein, S. Economics of converting renewable power to hydrogen. *Nat. Energy* **2019**, *4*, 216–222.

[5] Strmcnik, D.; Uchimura, M.; Wang, C.; Subbaraman, R.; Danilovic, N.; van der Vliet, D.; Paulikas, A. P.; Stamenkovic, V. R.; Markovic, N. M. Improving the hydrogen oxidation reaction rate by promotion of hydroxyl adsorption. *Nat. Chem.* **2013**, *5*, 300–306.

[6] Tang, T.; Liu, X. Z.; Luo, X.; Xue, Z. Z.; Pan, H. R.; Fu, J. J.; Yao, Z. C.; Jiang, Z.; Lyu, Z. H.; Zheng, L. R. et al. Unconventional bilateral compressive strained Ni–Ir interface synergistically accelerates alkaline hydrogen oxidation. *J. Am. Chem. Soc.* **2023**, *145*, 13805–13815.

[7] Zhao, R. P.; Yue, X.; Li, Q. H.; Fu, G. T.; Lee, J. M.; Huang, S. M. Recent advances in electrocatalysts for alkaline hydrogen oxidation reaction. *Small* **2021**, *17*, 2100391.

[8] Setzler, B. P.; Zhuang, Z. B.; Wittkopf, J. A.; Yan, Y. S. Activity targets for nanostructured platinum-group-metal-free catalysts in hydroxide exchange membrane fuel cells. *Nat. Nanotechnol.* **2016**, *11*, 1020–1025.

[9] Gao, F. Y.; Liu, S. N.; Ge, J. C.; Zhang, X. L.; Zhu, L.; Zheng, Y. R.; Duan, Y.; Qin, S.; Dong, W. X.; Yu, X. X. et al. Nickel-molybdenum-niobium metallic glass for efficient hydrogen oxidation in hydroxide exchange membrane fuel cells. *Nat. Catal.* **2022**, *5*, 993–1005.

[10] Zhang, B. H.; Zhao, G. Q.; Zhang, B. X.; Xia, L. X.; Jiang, Y. Z.; Ma, T. Y.; Gao, M. X.; Sun, W. P.; Pan, H. G. Lattice-confined Ir clusters on Pd nanosheets with charge redistribution for the hydrogen oxidation reaction under alkaline conditions. *Adv. Mater.* **2021**, *33*, 2105400.

[11] Liao, Y. R.; Wang, S. C.; Zhang, Y. F.; Zhang, Y.; Gao, Y.; Mu, X. Q.; Liu, S. L.; Wang, D. S.; Dai, Z. H. Advances in the study of HOR reaction mechanisms under alkaline conditions. *Adv. Sens. Energy Mater.* **2024**, *3*, 100089.

[12] Wang, H. S.; Abruña, H. D. Rh and Rh alloy nanoparticles as highly active H_2 oxidation catalysts for alkaline fuel cells. *ACS Catal.* **2019**, *9*, 5057–5062.

[13] Wang, J. M.; Zhang, B. X.; Zheng, X. Z.; Liu, X. R.; Guo, W.; Luo, Z. X.; Liu, Y. F.; Gao, M. X.; Chen, J.; Zhuang, Z. B. et al. Pt single atoms coupled with Ru nanoclusters enable robust hydrogen oxidation for high-performance anion exchange membrane fuel cells. *Nano Res.* **2024**, *17*, 6147–6156.

[14] Zhou, Y.; Kuang, Y. B.; Hu, G. Z.; Wang, X.; Feng, L. G. An effective Pt–CoTe/NC catalyst of bifunctional methanol electrolysis for hydrogen generation. *Mater. Today Phy.* **2022**, *27*, 100831.

[15] Mu, X. Q.; Zhang, X. Y.; Chen, Z. Y.; Gao, Y.; Yu, M.; Chen, D.; Pan, H. Z.; Liu, S. L.; Wang, D. S.; Mu, S. C. Constructing symmetry-mismatched $Ru_xFe_{3-x}O_4$ heterointerface-supported Ru clusters for efficient hydrogen evolution and oxidation reactions. *Nano Lett.* **2024**, *24*, 1015–1023.

[16] Lu, S. Q.; Zhuang, Z. B. Investigating the influences of the adsorbed species on catalytic activity for hydrogen oxidation reaction in alkaline electrolyte. *J. Am. Chem. Soc.* **2017**, *139*, 5156–5163.

[17] Wang, Y. H.; Wang, X. T.; Ze, H. J.; Zhang, X. G.; Radjenovic, P. M.; Zhang, Y. J.; Dong, J. C.; Tian, Z. Q.; Li, J. F. Spectroscopic verification of adsorbed hydroxy intermediates in the bifunctional mechanism of the hydrogen oxidation reaction. *Angew. Chem., Int. Ed.* **2021**, *60*, 5708–5711.

[18] Zhang, X. Y.; Xiao, X. Z.; Chen, J.; Liu, Y. F.; Pan, H. G.; Sun, W. P.; Gao, M. X. Toward the fast and durable alkaline hydrogen oxidation reaction on ruthenium. *Energy Environ. Sci.* **2022**, *15*, 4511–4526.

[19] Han, L. L.; Ou, P. F.; Liu, W.; Wang, X.; Wang, H. T.; Zhang, R.; Pao, C. W.; Liu, X. J.; Pong, W. F.; Song, J. et al. Design of Ru–Ni diatomic sites for efficient alkaline hydrogen oxidation. *Sci. Adv.* **2022**, *8*, eabm3779.

[20] An, L. L.; Zhao, X.; Zhao, T. H.; Wang, D. L. Atomic-level insight into reasonable design of metal-based catalysts for hydrogen oxidation in alkaline electrolytes. *Energy Environ. Sci.* **2021**, *14*, 2620–2638.

[21] Ni, W. Y.; Meibom, J. L.; Hassan, N. U.; Chang, M.; Chu, Y. C.; Krammer, A.; Sun, S. L.; Zheng, Y. W.; Bai, L. C.; Ma, W. C. et al. Synergistic interactions between PtRu catalyst and nitrogen-doped carbon support boost hydrogen oxidation. *Nat. Catal.* **2023**, *6*, 773–783.

[22] Mao, J. J.; He, C. T.; Pei, J. J.; Liu, Y.; Li, J.; Chen, W. X.; He, D. S.; Wang, D. S.; Li, Y. D. Isolated Ni atoms dispersed on Ru nanosheets: High-performance electrocatalysts toward hydrogen oxidation reaction. *Nano Lett.* **2020**, *20*, 3442–3448.

[23] Duan, Y.; Yu, Z. Y.; Yang, L.; Zheng, L. R.; Zhang, C. T.; Yang, X. T.; Gao, F. Y.; Zhang, X. L.; Yu, X. X.; Liu, R. et al. Bimetallic nickel-molybdenum/tungsten nanoalloys for high-efficiency hydrogen oxidation catalysis in alkaline electrolytes. *Nat. Commun.* **2020**, *11*, 4789.

[24] Wang, Y.; Yang, Y.; Jia, S. F.; Wang, X. M.; Lyu, K. J.; Peng, Y. Q.; Zheng, H.; Wei, X.; Ren, H.; Xiao, L. et al. Synergistic Mn–Co catalyst outperforms Pt on high-rate oxygen reduction for alkaline polymer electrolyte fuel cells. *Nat. Commun.* **2019**, *10*, 1506.

[25] Wang, X. D.; Liu, X. R.; Fang, J. J.; Wang, H. P.; Liu, X. W.; Wang, H. Y.; Chen, C. J.; Wang, Y. S.; Zhang, X. J.; Zhu, W. et al. Tuning the apparent hydrogen binding energy to achieve high-performance Ni-based hydrogen oxidation reaction catalyst. *Nat. Commun.* **2024**, *15*, 1137.

[26] Zhao, J.; Zhang, Y. X.; Zhuang, Z. C.; Deng, Y. T.; Gao, G.; Li, J. Y.; Meng, A. L.; Li, G. C.; Wang, L.; Li, Z. J. et al. Tailoring d–p orbital hybridization to decipher the essential effects of heteroatom substitution on redox kinetics. *Angew. Chem., Int. Ed.* **2024**, *63*, e202404968.

[27] Liu, J. Y.; Kong, X.; Zheng, L. R.; Guo, X.; Liu, X. F.; Shui, J. L. Rare earth single-atom catalysts for nitrogen and carbon dioxide reduction. *ACS Nano* **2020**, *14*, 1093–1101.

[28] Wang, X.; Tang, Y. W.; Lee, J. M.; Fu, G. T. Recent advances in rare-earth-based materials for electrocatalysis. *Chem Catal.* **2022**, *2*, 967–1008.

[29] Zhang, S.; Zeng, Z. C.; Li, Q. Q.; Huang, B. L.; Zhang, X. Y.; Du, Y. P.; Yan, C. H. Lanthanide electronic perturbation in Pt–Ln (La, Ce, Pr and Nd) alloys for enhanced methanol oxidation reaction activity. *Energy Environ. Sci.* **2021**, *14*, 5911–5918.

[30] Escudero-Escribano, M.; Malacrida, P.; Hansen, M. H.; Vej-Hansen, U. G.; Velázquez-Palenzuela, A.; Tripkovic, V.; Schiøtz, J.; Rossmeisl, J.; Stephens, I. E. L.; Chorkendorff, I. Tuning the activity

of Pt alloy electrocatalysts by means of the lanthanide contraction. *Science* **2016**, *352*, 73–76.
[31] Zhu, S. Y.; Sun, M. Z.; Mei, B. B.; Yang, L. T.; Chu, Y. Y.; Shi, Z. P.; Bai, J. S.; Wang, X.; Jiang, Z.; Liu, C. P. et al. Intrinsic spin shielding effect in platinum-rare earth alloy boosts oxygen reduction activity. *Natl. Sci. Rev.* **2023**, *10*, nwad162.
[32] Qin, Y. L.; Yu, K. D.; Wang, G.; Zhuang, Z. C.; Dou, Y. H.; Wang, D. S.; Chen, Z. B. Adjacent-ligand tuning of atomically precise Cu−Pd sites enables efficient methanol electrooxidation with a CO-free pathway. *Angew. Chem., Int. Ed.* **2025**, *64*, e202420817.
[33] Yang, J. R.; Zhu, C. X.; Li, W. H.; Zheng, X. S.; Wang, D. S. Organocatalyst supported by a single-atom support accelerates both electrodes used in the chlor-alkali industry via modification of non-covalent interactions. *Angew. Chem. Int. Ed.* **2024**, *63*, e202314382.
[34] Zhuang, J. H.; Wang, D. S. Recent advances of single-atom alloy catalyst: Properties, synthetic methods and electrocatalytic applications. *Mater. Today Catal.* **2023**, *2*, 100009.
[35] Wang, Y.; Ma, F. Y.; Zhang, G. Q.; Zhang, J. W.; Zhao, H.; Dong, Y. M.; Wang, D. S. Precise synthesis of dual atom sites for electrocatalysis. *Nano Res.* **2024**, *17*, 9397–9427.
[36] Mu, X. Q.; Liu, S. L.; Zhang, M. Y.; Zhuang, Z. C.; Chen, D.; Liao, Y. R.; Zhao, H. Y.; Mu, S. C.; Wang, D. S.; Dai, Z. H. Symmetry-broken Ru nanoparticles with parasitic Ru–Co dual-single atoms overcome the volmer step of alkaline hydrogen oxidation. *Angew. Chem., Int. Ed.* **2024**, *63*, e202319618.
[37] Niu, W. H.; Marcus, K.; Zhou, L.; Li, Z.; Shi, L.; Liang, K.; Yang, Y. Enhancing electron transfer and electrocatalytic activity on crystalline carbon-conjugated g-C_3N_4. *ACS Catal.* **2018**, *8*, 1926–1931.
[38] Cheng, J. J.; Hou, Y. C.; Lian, K. K.; Xiao, H. X.; Lin, S.; Wang, X. C. Metalized carbon nitrides for efficient catalytic functionalization of CO_2. *ACS Catal.* **2022**, *12*, 1797–1808.
[39] Zheng, X. B.; Cui, P. X.; Qian, Y. M.; Zhao, G. Q.; Zheng, X. S.; Xu, X.; Cheng, Z. X.; Liu, Y. Y.; Dou, S. X.; Sun, W. P. Multifunctional active-center-transferable platinum/lithium cobalt oxide heterostructured electrocatalysts towards superior water splitting. *Angew. Chem., Int. Ed.* **2020**, *59*, 14533–14540.
[40] Li, P.; Zhao, G. Q.; Cui, P. X.; Cheng, N. Y.; Lao, M. M.; Xu, X.; Dou, S. X.; Sun, W. P. Nickel single atom-decorated carbon nanosheets as multifunctional electrocatalyst supports toward efficient alkaline hydrogen evolution. *Nano Energy* **2021**, *83*, 105850.
[41] Zhong, H. X.; Zhang, Q.; Wang, J.; Zhang, X. B.; Wei, X. L.; Wu, Z. J.; Li, K.; Meng, F. L.; Bao, D.; Yan, J. M. Engineering ultrathin C_3N_4 quantum dots on graphene as a metal-free water reduction electrocatalyst. *ACS Catal.* **2018**, *8*, 3965–3970.
[42] Chen, Y. P.; Zheng, X. S.; Cai, J. Y.; Zhao, G. Q.; Zhang, B. X.; Luo, Z. X.; Wang, G. M.; Pan, H. G.; Sun, W. P. Sulfur doping triggering enhanced Pt–N coordination in graphitic carbon nitride-supported Pt electrocatalysts toward efficient oxygen reduction reaction. *ACS Catal.* **2022**, *12*, 7406–7414.
[43] Ruan, J. F.; Chen, Y. P.; Zhao, G. Q.; Li, P.; Zhang, B. X.; Jiang, Y. Z.; Ma, T. Y.; Pan, H. G.; Dou, S. X.; Sun, W. P. Cobalt single atoms enabling efficient methanol oxidation reaction on platinum anchored on nitrogen-doped carbon. *Small* **2022**, *18*, 2107067.
[44] Wang, M. M.; Wang, M. J.; Zhan, C. H.; Geng, H. B.; Li, Y. H.; Huang, X. Q.; Bu, L. Z. Ultrafine platinum-iridium distorted nanowires as robust catalysts toward bifunctional hydrogen catalysis. *J. Mater. Chem. A* **2022**, *10*, 18972–18977.
[45] Ju, W.; Bagger, A.; Hao, G. P.; Varela, A. S.; Sinev, I.; Bon, V.; Roldan Cuenya, B.; Kaskel, S.; Rossmeisl, J.; Strasser, P. Understanding activity and selectivity of metal-nitrogen-doped carbon catalysts for electrochemical reduction of CO_2. *Nat. Commun.* **2017**, *8*, 944.
[46] Kuang, P. Y.; Ni, Z. R.; Zhu, B. C.; Lin, Y.; Yu, J. G. Modulating the d-band center enables ultrafine Pt_3Fe alloy nanoparticles for pH-universal hydrogen evolution reaction. *Adv. Mater.* **2023**, *35*, 2303030.
[47] Niu, H. J.; Huang, C. X.; Sun, T.; Fang, Z.; Ke, X. X.; Zhang, R. M.; Ran, N.; Wu, J. B.; Liu, J. J.; Zhou, W. Enhancing Ni/Co activity by neighboring Pt atoms in NiCoP/MXene electrocatalyst for alkaline hydrogen evolution. *Angew. Chem., Int. Ed.* **2024**, *63*, e202401819.
[48] Li, X.; Han, X.; Yang, Z. R.; Wang, S.; Yang, Y.; Wang, J.; Chen, J. D.; Chen, Z. W.; Jin, H. L. Lattice-distorted Pt wrinkled nanoparticles for highly effective hydrogen electrocatalysis. *Nano Res.* **2024**, *17*, 3819–3826.